RSC Advances

PAPER

View Article Online
View Journal | View Issue

Cite this: *RSC Adv.*, 2023, **13**, 790

Hectorite-CTAB–alginate composite beads for water treatment: kinetic, isothermal and thermodynamic studies

Asranudin,[af] Holilah,[bf] Adi Setyo Purnomo, *[a] Hasliza Bahruji,[c] Dalia Allouss,[d] Ilias El Alaoui-Elbalrhiti,[e] Riki Subagyo,[a] Alya Awinatul Rohmah[a] and Didik Prasetyoko *[a]

Received 2nd November 2022
Accepted 19th December 2022

DOI: 10.1039/d2ra06934b

rsc.li/rsc-advances

Encapsulation of hectorite-modified CTAB with Ca-alginate formed reusable adsorbent beads for wastewater treatment. The thermogravimetric analysis (TGA) investigation indicated excellent thermal stability results for BHec-40 compared to Hec-40. Although the mesoporous surface area of BHec-40 decreased to 79.74 $m^2\ g^{-1}$ compared to 224.21 $m^2\ g^{-1}$ for Hec-40, the hectorite-CTAB–alginate beads showed high adsorption capacity and stability for methyl orange (MO) adsorption with more than 60% removal after five adsorption–desorption cycles. The influence of pH (3–11), temperature (30, 40, and 50 °C), initial concentration (50–400 mg L^{-1}), and contact time were studied to obtain the kinetics and thermodynamics of adsorption. The outcomes revealed a maximum monolayer adsorption capacity of 117.71 mg g^{-1} for BHec-40. The kinetics of adsorption demonstrated the suitability of using the pseudo-first-order kinetic model, while the equilibrium adsorption data follows the Langmuir isotherm. Thermodynamic analysis indicates physisorption of MO onto BHec-40. BHec-40 improves the reusability as an adsorbent for the removal of anionic dyes from aqueous media.

Introduction

The toxicity of azo dye (–N=N–) waste in the aquatic ecosystem is harmful to all water-using organisms[1]. A high concentration of dyes reduces the amount of dissolved oxygen, eventually increasing the release of toxic aromatic amine intermediates from anaerobic degradation.[2–5] Methyl orange degrades into intermediate products such as sulfonamides, aniline, *N′N* dimethyl benzyl-1,4-diamine, benzenesulfonic acid, and 1,4-diaminobenzene, which exhibit acute toxicity, and corrosive, carcinogenic and mutagenic properties.[6] Since synthetic dyes are resistant to biodegradation, a multitude of studies investigated their removal using electrocoagulation,[7] flocculation,[8] filtration,[9] chemical oxidation,[10] electrochemistry,[11] and ozone treatment.[12] The adsorption method prevents the conversion of methyl orange into toxic intermediates while offering effective, inexpensive recovery of the synthetic dye.[13,14]

Hectorite is a 2 : 1 smectite clay with exceptional properties as an adsorbent for metal ions and cationic dyes.[15,16] Hectorite adsorption behavior comes from the oxygen deformity of Mg–O octahedra and Si–O tetrahedra.[17] Hectorite is occurred naturally, although the presence of impurities requires pretreatment before can be used as adsorbent.[18] Hectorite can be synthesized from lithium (LiF or LiCl), magnesium (MgOH), and silica (SiO_2) in a molar ratio of 0.266 : 1.00 : 1.52, under controlled rates and low temperatures.[17,19,20] Inorganic cations on the surface can be modified through ion exchange with organic cations to form organophilic adsorbents.[21] Hectorite modified with cetyltrimethyl ammonium bromide increased the removal of Congo red and reactive orange 122.[22,23] However, the reusability of hectorite is restricted by its powdery form, which is difficult to recover from the media after adsorption, particularly when it involves recovery from a sewage treatment plant.[22,23] Transformation of adsorbent into hydrogel beads *via* immobilization into the sodium alginate (NA) polymer is promising approach to increase reusability. NA has significant stability in organic solvents, is flexible to extreme operation conditions, is readily biodegradable, harmless, inexpensive, as well as it produces hydrogels through crosslinking mechanisms with divalent cations.[24,25] NA has been used to immobilize activated charcoal, bentonite, gelatin, montmorillonite, kaolin, and microcrystalline cellulose for dye adsorption.[13,24–28]

[a]*Department of Chemistry, Institut Teknologi Sepuluh Nopember (ITS), Surabaya, 60111, Indonesia. E-mail: adi_setyo@chem.its.ac.id; didikp@chem.its.ac.id*

[b]*Research Center for Biomass and Bioproducts, National Research and Innovation Agency of Indonesia (BRIN), Cibinong, 16911, Indonesia*

[c]*Centre of Advanced Material and Energy Sciences, Universiti Brunei Darussalam, Gadong, Bandar Seri Begawan, 1410, Brunei Darussalam*

[d]*Laboratoire de Matériaux, Catalyse et Valorisation des Ressources Naturelles, Faculté des Sciences et Techniques, Hassan II University, 19, Casablanca, Marocco*

[e]*Department of Chemical & Biotechnological Engineering, Université de Sherbrooke, Québec, J1K 2R1, Canada*

[f]*Department of Food Science and Technology, Faculty of Agriculture, Halu Oleo University, Kendari, 93231, Indonesia*

Immobilized adsorbent powder improved the regeneration of adsorbent when used in both batch and dynamic systems.[13,29]

In this study, hectorite-CTAB was synthesized and immobilized into hydrogel beads *via* sodium alginate *via* ionotropic gelation. Ca^{2+} ions play a role of a physical crosslinking agent. The efficiency of hectorite-CTAB hydrogel bead was evaluated for methyl orange (MO) dye adsorption in a static system. Several operating parameters provide data on adsorption kinetics, isotherms, and thermodynamics, including adsorbent selection, contact time, and temperature effect. The adsorbent regeneration was determined to validate the feasibility of a large-scale application.

Experimental

Materials

Calcium chloride (≥99%), lithium chloride (≥99.99%), cetyltrimethylammonium bromide (≥98%), magnesium hydroxide (≥97.50%), sodium hydroxide (≥99%), and methyl orange were supplied by Merck. Colloidal silica (Ludox HS-40); was supplied by Sigma-Aldrich (Singapore). Na-alginate was provided by Himedia (MB1140). All chemicals utilised were of analytical grade.

Preparation of hectorite-CTAB–alginate (BHec-40)

Synthetic hectorite was prepared with reactants in the molar ratios of $LiCl : Mg(OH)_2 : SiO_2 = 0.798 : 3.00 : 4.56$.[18,19] The mixture of $LiCl : Mg(OH)_2 : SiO_2$ was refluxed for 6 h to produce homogeneous mixture. Cetyltrimethylammonium bromide (CTAB) surfactant at different ratios *i.e.* 5–40% (w/w) was added to the homogeneous mixture. The reflux was continued for 48 hours at 95 °C. The final product was washed using demineralization water and dried for 12 hours at 110 °C. Composite beads were prepared by mixing hectorite suspension (4 grams/25 mL) with 2% (w/v) Na-alginate slurry and stirring for 2 hours. The resulting composite slurry was released into a $CaCl_2$ solution (2%) using a 15 mL syringe under continuous agitation and soaked in the $CaCl_2$ solution for 12 hours. The wet beads formed were 3–3.5 mm in size, dried using a −40 °C freezer for 5 hours to produce dry beads with an average size of 1–1.5 mm. The obtained beads are denoted BHec-40, and an illustration of the fabrication is shown in Fig. 1. For comparison, hectorite beads without CTAB addition were also prepared and marked as BHec-0.

Physico-chemical characterization

X-ray diffraction (XRD) patterns were obtained from a PHILIPS-binary Xpert X-ray instrument employing Cu Kα1 radiation at 40 kV, the wavelength of 1.5405 nm, 30 mA. The data was obtained in a 2θ from 5 to 100° with a scanning rate of 1.02° per minute. The spectra of FTIR beads were characterized using an FTIR Spectrophotometer (Shimadzu Instrument Spectrum One 8400S) in the form of KBr pellets. Bead morphology was obtained using Scanning Electron Microscopy (Hitachi, FlexSEM 1000). Thermal analysis was performed using a simultaneous DTA/DTG thermal analyzer instrument (Sciences STA7200). The sample was heated from 28 to 900 °C at a rate of 10 °C min^{-1} under a nitrogen stream of 60 mL min^{-1}. Surface and pore area analysis on samples was performed using the Quantachrome Touchwin v1.11 instrument.

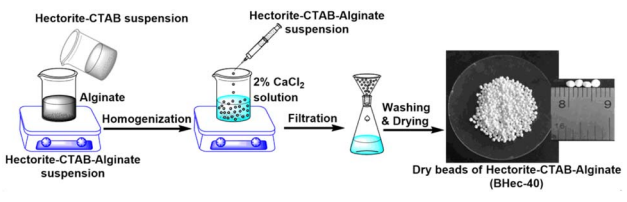

Fig. 1 Illustrative of preparation methodology for hectorite-CTAB–alginate (BHec-40).

Adsorption studies

Experiments on batch adsorption analyzed the adsorption behavior of MO on synthesized BHec-40. Various physico-chemical parameters were investigated on MO removal, including the effect of adsorbent at varying CTAB loading (BHec-5 to 40), variable pH of MO solution (3–11),[30] MO initial concentration (50–400 mg L^{-1}), contact time (10–140 min), and adsorbent dosage (0.5–3.0 g L^{-1}). MO solution (20 mL) was added with 50 mg dried adsorbent to obtain 2.5 g L^{-1} of BHec-40 in MO solution. All batch sorption processes were carried out using an automatic shaker at 30 °C for 140 minutes to achieve equilibrium. The dye concentration was measured by a UV-vis spectrophotometer (G-10S) at λ_{max} 465 nm. The maximum adsorption capacity of MO (q_e; mg g^{-1}) at equilibrium and the removal was calculated using eqn (1) and (2), respectively.

$$q_e = (C_o - C_e) \times \frac{V}{m} \quad (1)$$

C_o is MO's initial concentration (mg L^{-1}), and C_e is the equilibrium liquid-phase concentration (mg L^{-1}). V denotes the volume of the solution, and m denotes the mass of the adsorbent.

$$\text{Removal } (\%) = \frac{C_o - C_e}{C_o} \times 100 \quad (2)$$

Five adsorption–desorption cycles were conducted in reusability studies. After the adsorption was completed, the beads were washed with methanol to remove the adsorbed MO. The MO concentration was determined in the eluent from each cycle to obtain the desorption efficiency. The pH_{pzc} analysis was conducted by adding 2.5 g of BHec-40 into a series of acidic solutions (20 mL) at the $pH_i = 3$–11, and occasionally stirred at 303 K at 72 hours. The final pH (pH_f) of solutions were measured followed by plotting ΔpH ($pH_f - pH_i$) against pH_i. The pH_i at $\Delta pH = 0$ gave the pH_{pzc} value.[30]

Adsorption kinetics

The adsorption kinetics model was determined to describe the adsorption process and features. Adsorption capacities at different contact durations were analysed to derive the non-linear pseudo-first-order (eqn (3)) and non-linear pseudo-second-order (eqn (4)).[1,27,31]

$$q_t = q_e(1 - e^{-K_1 t}) \quad (3)$$

$$q_t = \frac{K_2 t q_e^2}{1 + tK_2 q_e} \quad (4)$$

where q_t and q_e are the MO adsorption capacities (mg g^{-1}) at time, t (min) and equilibrium, respectively. In comparison, the rate constants for the pseudo-first and pseudo-second order models are symbolized by K_1 and K_2, respectively. Furthermore, the R^2 coefficient was applied in order to evaluate the appropriateness of the kinetic adsorption models. The highest R^2 value close to one indicates that the kinetic adsorption suitability is greater.[18]

Adsorption isotherms

The results of adsorption at different concentrations were used to calculate the nonlinear isotherm. The following equation was employed to determine the Langmuir, Freundlich, Temkin, and Sips non-linear isotherm models (eqn (5)–(8)):[1,31]

$$q_e = \frac{q_m K_L C_e}{1 + K_L C_e} \quad (5)$$

$$q_e = K_f C_e^{1/n} \quad (6)$$

$$q_e = \frac{RT}{B} \ln K_T + \frac{RT}{B} \ln C_e \quad (7)$$

$$q_e = \frac{q_m K_s C_e^{ms}}{1 + K_s C_e^{ms}} \quad (8)$$

where K_L (L mg^{-1}), K_F (mg g^{-1}(L^{-1} mg^{-1})$1/n^{-1}$), and K_T (L mg^{-1}) are the isotherm constant of Langmuir, Freundlich, and Temkin, respectively. While q_m represents the maximum adsorption capacity of Langmuir, q_e is the adsorption capacity (mg g^{-1}), and C_e is the concentration (mg L^{-1}) of the methyl orange at equilibrium. Furthermore, n was the dimensionless constant that indicates the affinity of MO adsorption to the adsorbents, and B was the Temkin constant associated with the heat of MO adsorption.[1,31,32] The Langmuir isotherm has a dimensionless, essential feature called the Langmuir equilibrium parameter R_L, defined by eqn (9).[24]

$$R_L = \frac{1}{1 + K_L C_o} \quad (9)$$

Statistical analysis

Values of coefficient (R^2), residual sum of squares (RSS), and chi-square (χ^2) were used to evaluate the adsorption capacities of the kinetic and isotherm studies. The RSS and χ^2 can be defined by the following eqn (10) and (11):[1,26,33]

$$\mathrm{RSS} = \sum_{i=1}^{n} \left(q_{exp,} - q_{cal,}\right)_i^2 \quad (10)$$

$$\chi^2 = \sum_{i=1}^{n} \frac{\left(q_{exp} - q_{cal}\right)^2}{q_{cal}} \quad (11)$$

where q_{exp} is the adsorption capacity at time t (min), q_{cal} is the adsorption capacity obtained from the isotherm model, and n is the number of experiments. The RSS and χ^2 error function were used to analyze the model that best fit the experimental data for the kinetic and isotherm models. A lower RSS and χ^2 shows the best model fit.[1,32,34]

Adsorption thermodynamic

The thermodynamic aspect of MO adsorption towards BHec-40 can be determined by the adsorption enthalpy (ΔH; kJ mol^{-1}), adsorption entropy (ΔS; J mol^{-1} K^{-1}), and adsorption free energy (ΔG; kJ mol^{-1}). Experiments were conducted at temperatures ranging from 30 to 50 °C. Eqn (12) describes the Arrhenius relationship, which was used to calculate the activation energy E_a (kJ mol^{-1}), Arrhenius constant A (g mg^{-1} min^{-1}), and coefficient of correlation R^2 using the pseudo-first-order constant K_1.

$$\ln K_1 = \ln A - \frac{E_a}{RT} \quad (12)$$

The Van't Hoff equation (eqn (13)) was used to calculate the thermodynamic adsorption parameters ($\Delta G°$, $\Delta H°$, and ΔS):[31,32]

$$\ln K_c = \frac{\Delta S^\circ}{R} - \frac{\Delta H^\circ}{RT} \quad (13)$$

The enthalpy and entropy of MO adsorption can be calculated by plotting $\ln K_c$ and $1/T$. The slope of the graph shows the value of $\Delta H/R$, while the intercept will show the value of $\Delta S/R$ so that the enthalpy and entropy of MO adsorption can be calculated.[35]

$$\Delta G^\circ = -RT \ln K_c = \Delta H^\circ - T\Delta S^\circ \quad (14)$$

where T, R, and K_c are the adsorption temperature (K), the gas constant (8.3145 J mol^{-1} K^{-1}), and the K_c is the equilibrium constant.

Results and discussion

Characterization of hectorite–alginate bead composite

Structural analysis. The X-ray diffraction (XRD) pattern of Hec-40 and BHec-40 beads were presented in Fig. 2. Hectorite peaks were detected at 5.64°, 19.63°, 34.53°, 60.55° and 72.08° for (001), (110, 020), (130, 200), (150, 240, 310), and (060, 330) diffraction planes, respectively.[36–38] There were no peaks in the hectorite profile at $2\theta = 4.77°$ and 22.8° for the consistent reflections of magnesium hydroxide mineral brucite and amorphous silica, respectively, confirming that all of the $Mg(OH)_2$ and silica were transformed to hectorite structure.[18] Hectorite-40% CTAB powder shows d_{001} lattice value at 1.450 nm, indicating the presence of interlayer cations with a high layer charge.

The XRD pattern of hectorite beads presented a considerable shift in [001] peak from $2\theta = 5.64°$ to lower 2θ values of 5.01°. The shift implied an increase in the interlayer space of hectorite from 1.450 nm to 1.76 nm after being composited with calcium alginate. The alginate molecules are suggested to intercalate

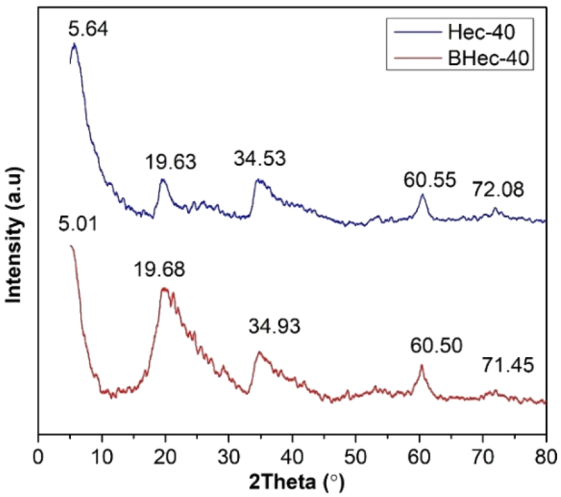

Fig. 2 The XRD pattern of Hec-40 and BHec-40.

into the interlayer spaces of Hec-40, consequently expanding the interlayer distances.

Fourier transform infrared spectroscopy (FTIR). The alginate, Hec-40 and BHec-40 beads spectra were presented in Fig. 3. BHec-40 displayed the typical bands of hectorite at 457, 661, 1006, 1479, 1546, 1627, and 3427 cm^{-1}.[39] The absorption band at 3427 cm^{-1} was attributed to the hydroxyl stretching vibration of H_2O. Moreover, two unique peaks related to Si–O stretching (1006 cm^{-1}) and water deformation vibrations between layers (661 cm^{-1} and 1641 cm^{-1}) were detected in hectorite.[20,22,39] The symmetric stretching of Mg–O was observed at 457 cm^{-1}, which corresponded to the octahedral units of hectorite-type clay minerals.[15] The incorporation of CTAB to Hec-40 and BHec-40 produced asymmetric and symmetric C–H strain vibrations of the CTAB at 2924 and 2850 cm^{-1}, respectively.[15,22,40,41] Furthermore, the pure alginate presented typical broad bands at 3437 cm^{-1} (OH stretching). In addition, the crosslinking in beads is liable for shifting the wavenumber of the carboxyl peak from 1615 cm^{-1} (C=O group) to 1627 cm^{-1} or

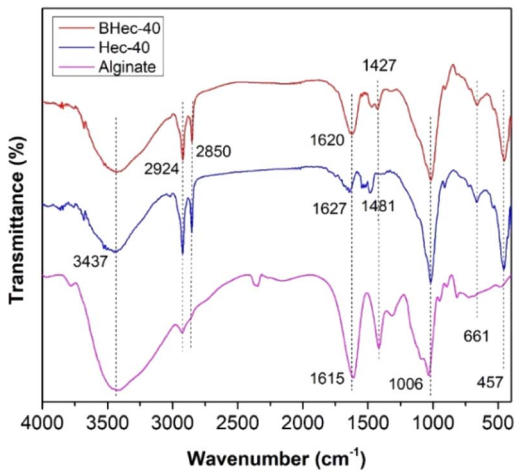

Fig. 3 The FTIR spectra of alginate, Hec-40 and BHec-40.

1620 (COO-asymmetric stretching), representing the appearance of intermolecular hydrogen bridges.[42] The band at 1427 represents the presence of ν(C–OH).[43]

Morphological analysis. Scanning electron microscopy (SEM) analysis of BHec-0, BHec-40 and Hec-40 powder were illustrated in Fig. 4. The dried beads with ~1 mm diameter were formed on BHec-40 (Fig. 4a) that was composed of hectorite modified CTAB and alginate. The beads formed from hectorite without CTAB (BHec-0) also showed a similar large diameter, although the beads appeared less smooth on the edges (Fig. 4c). Scanning at a higher-resolution shows that the surface morphology of hectorite beads differs from the hectorite powder due to the alginate-intercalation in hectorite. BHec-40 and BHec-0 revealed a network-type linkage, confirming the encapsulation of hectorite within the alginate network (Fig. 4b). The alginate moieties transformed the non-uniform hectorite powder (Fig. 4e) into compact and rigid network structures.[44] The elemental analysis of BHec-0 and BHec-40 was presented in Table 1. The difference in the elemental composition of these two beads is that there is no N element in BHec-0 because BHec-0 uses hectorite unmodified CTAB. Elemental nitrogen is derived from the CTAB surfactant.

Thermal analysis. Thermal analysis of Hec-40 and BHec-40 were carried out using the TGA/DTA analysis as shown in Fig. 5. Hec-40 powder presented four decomposition stages. The 1st step ensues at lower temperatures (<200 °C) and conforms to the dehydration of water. The breakdown of the cationic surfactant that was physically adsorbed onto the hectorite surface led to the 2nd step that occur between 200 and 350 °C (250 °C). The 3rd step at 370–440 °C was generated by surfactant dehydration in the hectorite interlayer spacing. The dehydroxylation process is the fourth stage occurred between 600 to 734 °C.[40,45]

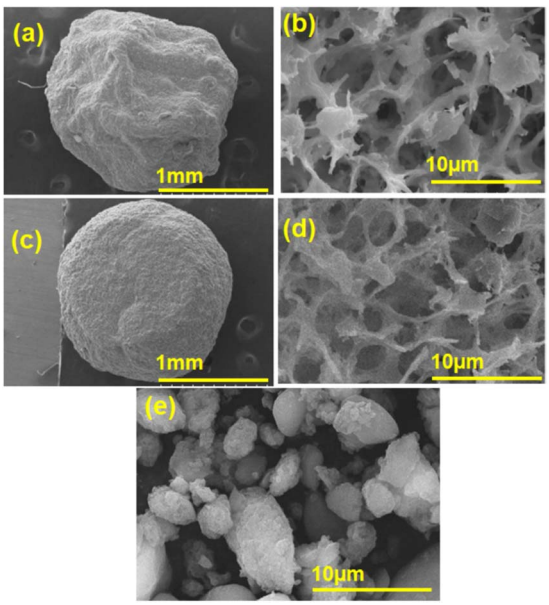

Fig. 4 SEM image of BHec-0 (a and b), BHec-40 (c and d) and Hec 40 (e).

Table 1 The elemental content of BHec-0, BHec-40 and Hec-40 from EDS mapping

	Weight (%)		
Element	BHec-0	BHec-40	Hec-40
C	8.54	11.39	14.62
N	—	3.16	4.92
O	45.29	41.93	37.72
Na	0.99	2.01	—
Mg	6.71	8.08	14.48
Si	11.88	14.41	24.89
Cl	9.28	7.83	3.38
Ca	17.31	11.18	—

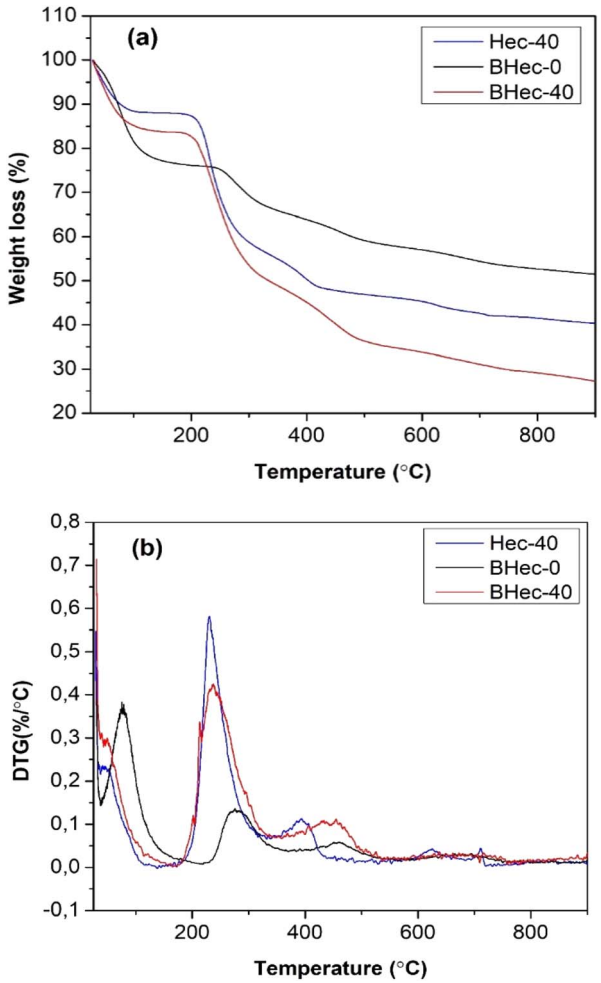

Fig. 5 TGA (a) and DTG (b) curves of Hec-40, BHec-0 and BHec-40.

The thermogravimetric curve of BHec-40 represents three decomposition stages with T_{max} peaks at 50.10 °C, 234.01 °C and 450.51 °C (Table 2). Degradation is caused by the dehydration of coordinated water molecules and the breakdown of glycoside bonds between 50 and 200 °C. The second and third T_{max} peak shifted to high temperatures due to the degradation of alginate molecules in the beads. The degradation of alginate polymer ensues in more than one step, between 200–400 °C and 500–650 °C.[46] The BHec-40 is more stable than the Hec-40 powder. The solid residue of Hec-40 and BHec-40 were determined at 39.97% and 27.23%, respectively.

N_2 adsorption–desorption. N_2 adsorption–desorption isotherms of hectorite-40% CTAB powder and hectorite-40% CTAB bead is shown in Fig. 6. This analysis was executed to compare the pore characteristics of Hec-40 powder and bead shape. Hec-40 and Hec-40 bead showed the hysteresis loops in the range of 0.50–0.90 (P/P_o), conforming to the characteristics of type IV isotherms and mesoporous materials. The surface area of Hec-40 bead is lower than hectorite powder due to the intercalation of alginate species that have taken up residence on the hectorite interlayer surface and hectoritemesoporous.[18] The mesoporous surface area of Hec-40 powders, and bead were 224.21 $m^2\ g^{-1}$ and 79.74 $m^2\ g^{-1}$ respectively based on NDLFT method.

Batch sorption study

Beads selection. The beads produced form hectorite-CTAB–alginate composites *i.e.* Hectorite-bead (BHec), hectorite-CTAB5% bead (BHec-5), hectorite-CTAB10% bead (BHec-10), hectorite-CTAB20% bead (BHec-20), hectorite-CTAB30% bead (BHec-30), and hectorite-CTAB40% bead (BHec-40) were used in the adsorption of methyl orange dyes (Fig. 7). The BHec-10 to BHec-40 absorbed more than 90% methyl orange, with the BHec-40 having the highest absorption capacity of 19.69 mg g^{-1}. These results indicate that CTAB plays a vital role in increasing the number of cationic sites ($N^+(CH_3)_3$–R) on hectorite to absorb MO in an aqueous solution.[40] The pH_{pzc} analysis of BHec-40 showed the zeta potential of BHec-40 was determined at 33.4 ± 0.35 mV (Fig. 9). This positive zeta potential value indicates the positively charged BHec-40 surface, which implied the material adsorbed MO through electrostatic attraction[1]. Pure hectorite showed an inferior degree of removal (3.93%; 0.783 mg g^{-1}), because the naturally available sites were similar to those of the sulphate group ($-SO_3^-$) in MO.[1,47] Based on the value of capacity and degree of removal, it shows that BHec-40 has the best performance and was selected for further adsorption experiments.

Table 2 Summary of temperature peak and weight of residue at 900 °C of Hec-40, BHec-0, and BHec-40

Sample	$T_{P\text{-}1}$	$T_{P\text{-}2}$	$T_{P\text{-}3}$	$T_{P\text{-}4}$	$W_{loss T_{P_2}}$ (%)	$W_{loss T_{P_3}}$ (%)	$W_{residue}$ (%)
Hec-40	58.81	231.19	393.94	710.51	33.90	8.11	39.97
BHec-0	78.22	271.75	457.52	—	15.82	4.31	51.46
BHec-40	50.10	236.40	450.51	—	29.21	12.27	27.23

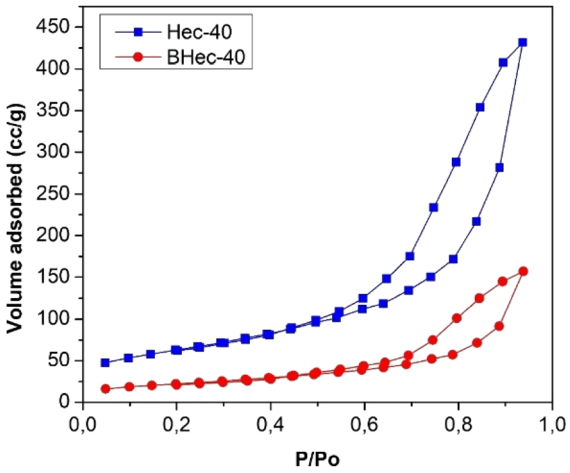

Fig. 6 N_2 adsorption–desorption curve of Hec-40 and BHec-40.

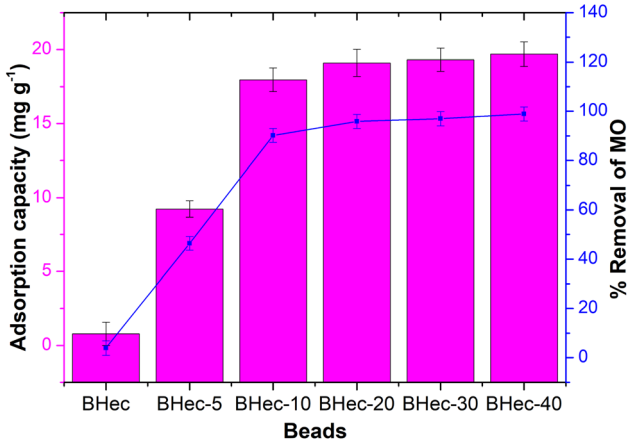

Fig. 7 Screening of beads (2.5 g L^{-1}, 20 mL, 50 mg L^{-1}).

pH, pH_{pzc} and beads dose effect. The molecular structure of methyl orange depends on the initial pH of the solution. Under acidic conditions, MO molecules are in the hydrazone structure, which causes the color of the solution to change to red-orange. At a neutral pH, MO is in the basic structure with yellow-orange color.[48–51] Fig. 8 shows the MO adsorption using BHec-40 in the range of pH 4–11, with the degree of MO removal achieved more than 98% at all pH conditions. In this study, the pH changes of the solution do not affect the adsorption of MO into the BHec-40, indicating that MO adsorption *via* physical interactions rather than chemical interactions. Changes in pH do not affect the active sites on CTAB-modified hectorite adsorbent.[22]

The ionization state of the adsorbate and the surface charge of the adsorbent are pH dependent. Therefore, the zero-point value of charge (pH_{pzc}) provides information on the pH range in which the surface of the adsorbent is positively or negatively charged.[13] The pH_{pzc} of BHec-40 was determined at 7.21, as shown in Fig. 9. This indicates that for pH > pH_{pzc} 7.21, the surface of BHec-40 is negatively charged, thereby appropriate for removing cationic dyes. However, at the pH value < pH_{pzc} 7.21, the surface of the adsorbent becomes positively charged.

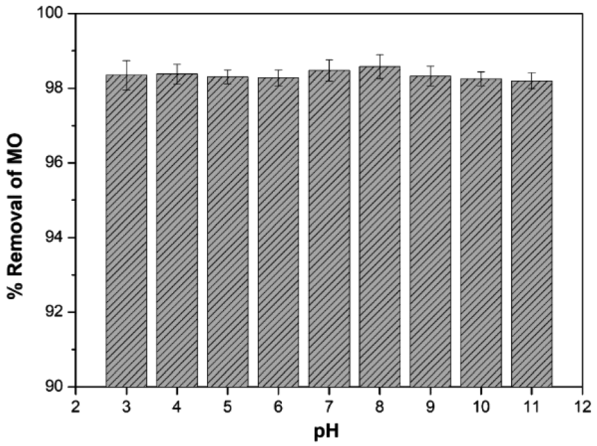

Fig. 8 Solution pH effect, where MO initial concentration (50 mg L^{-1}) 2.5 g L^{-1} beads at 25 ± 1 °C for 90 minutes.

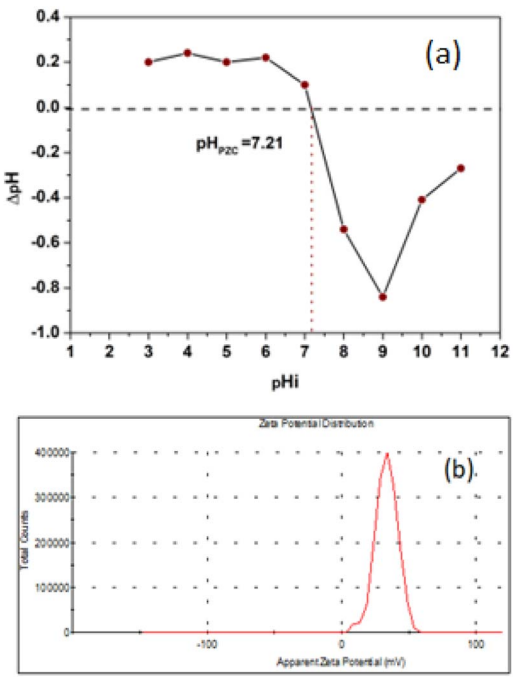

Fig. 9 (a) pH_{pzc} analysis of BHec-40, (b) zeta potential of BHec-40.

Since there are no significant differences in the MO removal efficiency with the pH variation, MO absorption occurred *via* physical interaction rather than chemical interaction on the charged surface of BHec-40.

The effect of adsorbent dosage on methyl orange removal showed that 98% MO removal was achieved using more than 2 g L^{-1} of adsorbent. Fig. 10 shows that 2.5–3 g L^{-1} is the optimum dose of adsorbent for MO removal in solution. In addition, Hec-40% beads at 1 g L^{-1} can adsorb more than 50% of MO. The increase in adsorbent dose could be associated with increased adsorption sites of CTAB, which interact electrostatically with the anion sites of the $-SO_3^-$ in MO. Moreover, increasing the adsorbent dose will increase the van der Waals attraction

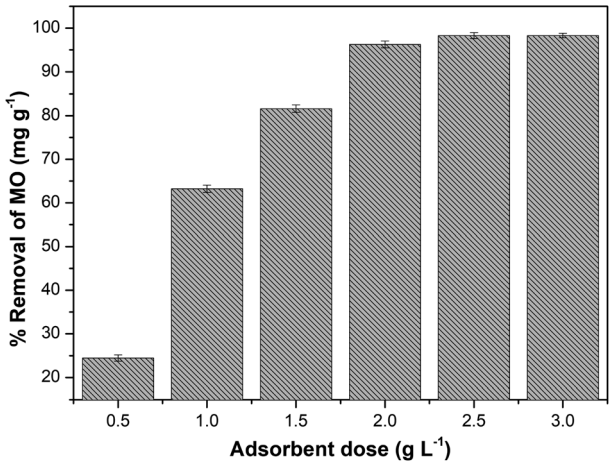

Fig. 10 Effect of beads dose (initial concentration 50 mg L^{-1}; at 25 ± 1 °C for 90 minutes).

between the MO phenyl ring and the $-CH_2^-$ group of CTAB *via* hydrogen bonding.[22]

Contact time effect and adsorption kinetics. The adsorption kinetic model provides insight into the mechanism of methyl orange adsorption on BHec-40. This study investigated the adsorption kinetics using the pseudo-first order and pseudo-second order models. Fig. 11 illustrates the influence of contact time and initial methyl orange concentration on methyl orange adsorption to the BHec-40. The amount of methyl orange adsorbed onto BHec-40 increased with the prolonged contact time, reaching equilibrium time in 90 min. Adsorption kinetics used the Lagergren model for the non-linear pseudo-first order and the pseudo-second-order models.[1,32,48,52]

Fig. 10 illustrates the pseudo-first order and pseudo-second-order non-linear plots of methyl orange adsorption using 50 mg L^{-1} initial concentration at 30 °C. The representative kinetic data were summarized in Table 3. The R^2 value of the pseudo-first-order is higher than the pseudo-second order, while the values of the pseudo-first order Residual Sum of Square (RSS) and reduced χ_c^2 are smaller than the pseudo-second order. The higher correlation coefficient (R^2) indicates that the pseudo-first-order model is a better fit for this adsorption. The fit of the model is supported by the value of the RSS and χ_c^2 error variables, which are smaller in pseudo-first order. According to the three statistical variables, the pseudo-first-order kinetic model fits the experimental data.[1,32,34,40,50,53]

Table 3 Kinetic parameters of methyl orange adsorption onto BHec-40

Kinetic parameters	First-order	Second-order
k	0.0307	0.0014
Q	20.1876	24.617
Adj. R^2	0.9517	0.9489
Residual sum of square (RSS)	5.0145	5.3024
Reduced chi-sqr (χ_c^2)	0.8357	0.8837

MO concentration effect and sorption isotherms. The effect of MO concentration on the adsorption capacity is shown on the isotherm plot of BHec-40 (Fig. 12). The adsorption process was performed at 30 °C, using the initial MO concentration ranging from 50 to 400 mg L^{-1}. The adsorption capacity of BHec-40 increased significantly at the initial concentration of 50–350 mg L^{-1}. However, at 400 mg L^{-1}, the beads experienced adsorption saturation, meaning the entire surface of the adsorbent was occupied with the adsorbates. To better understand the adsorption process on BHec-40, a plot of the sorption isotherm was carried out, namely the Langmuir isotherm, Freundlich isotherm, Temkin isotherm and Sips isotherm, as explained in Fig. 12. Table 4 summarises the evaluation of the model parameters of the MO adsorption isotherm into BHec-40.

Fig. 12 shows that the Langmuir isotherm fits the experimental data compared to the Freundlich, Temkin, and Sips isotherms. It can be assumed from these results that the MO adsorption process on BHec-40 involves monolayer adsorption on uniform binding sites, and there is no interaction between adsorbates to form multiple layers on the surface of the adsorbent.[1,17,21,22,32,52,54]

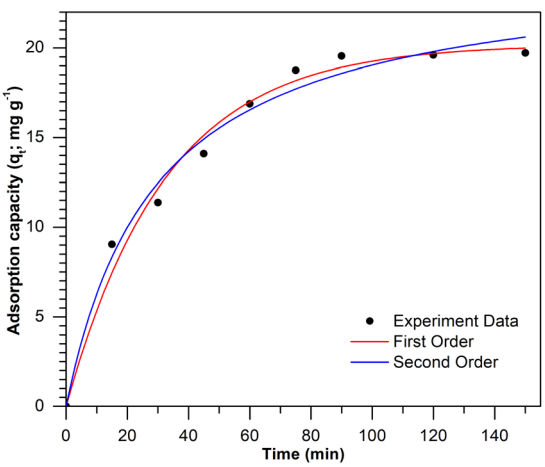

Fig. 11 The pseudo-first-order and pseudo-second-order kinetics for the adsorption of MO using BHec-40.

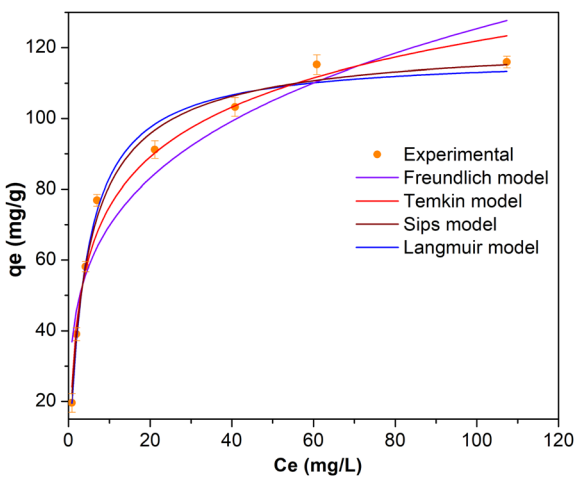

Fig. 12 The adsorption isotherms non-linear of MO onto BHec-40.

Table 4 Isotherm analysis of MO using BHec-40 at 30 °C by non-linear fitting method

			Error value		
Isotherm	Value		Adj. R^2	RSS	Red. chi-sqr
Langmuir	q_{max}	117.7145	0.98568	109.953	18.325
	K_L	0.2408			
Freundlich	K_F	38.7071	0.90274	746.580	124.43
	n	3.91834			
Temkin	K_T	3.968	0.98561	180.413	30.413
	B	20.3685			
Sips	q_S	122.6681	0.98561	92.071	18.414
	K_S	0.2605			
	m_s	0.8717			

Three error values, namely the correlation coefficient (R^2), Residual Sum of Square (RSS) and ${\chi_c}^2$ were determined to support the assumption of the adsorption process. Table 2 shows that the maximum monolayer adsorption capacity is 117.710 mg g^{-1}, the regression coefficient value (R^2) is the Langmuir isotherm (0.986) which is higher than the Temkin isotherm (0.976) and the Freundlich isotherm (0.902). The regression coefficient indicates that the adsorption of MO into BHec-40 has a strong correlation with the Langmuir isotherm.[1,55–58] In addition, the lowest RSS and ${\chi_c}^2$ error values are shown in the Sips and Langmuir isotherm, respectively.

Furthermore, to show that the MO adsorption process into BHec-40 is beneficial under the investigated conditions (30 °C), it can be determined based on the value of the equilibrium parameter (R_L) on the Langmuir isotherm.[59] In this study, the R_L value was 0.0756, which means that the adsorption conditions of MO into BHec-40 were favorable. The meaning value of $R_L > 1$ expresses unfavorable adsorption, while $0 < R_L < 1$ expresses favorable adsorption, $R_L = O$ expresses irreversible adsorption, and $R_L = 1$ expresses linear adsorption. In the Freundlich isotherm, there are important parameters to state the advisability of an adsorption process, where the value of the Freundlich constant in this study ($n = 3.918$) is more significant than one which indicates a favorable adsorption process.[18,34,41,50,53,55,60,61] The subsequent isotherm analysis is the Temkin isotherm. This isotherm has a factor that characterizes the interaction between the adsorbent and adsorbate and is used for heterogeneous surface energy systems. From the Temkin isotherm, two constants were obtained, namely the equilibrium binding constant of the Temkin isotherm (L g^{-1}) ($=K_T$) and the constant associated with the heat of absorption (J mol^{-1}) ($=b$). The calorific absorption value can be used to identify the adsorption mechanism. Physical adsorption occurs if the absorption heat value is less than 1 kcal mol^{-1}, while 20–50 kcal mol^{-1} values indicate chemical adsorption.[1,62–64] In this study, the calorific absorption value after conversion was 0.00486 kcal mol^{-1}, indicating that MO adsorption into BHec-40 was a physical process. In accordance with the nonlinear Langmuir isotherm model calculation, the maximum adsorption capacity of BHec-40 in this research was greater than that of the other adsorbents listed in Table 5. It shows the ability of BHec-40 as an effective MO dye adsorbent for aqueous solutions.

Table 5 The equilibrium adsorption capacities of MO on various adsorbents

Adsorbents	q_{max} (mg g^{-1})	Ref.
Modified coffee waste (MCWs)	62.50	50
Goethite (G)	55.00	65
Chitosan beads (CSB)	75.00	65
Goethite-chitosan beads (GCSB)	84.00	65
Chitosan/diatomite composite	35.12	66
Functionalized-CNTs loaded TiO_2 follows	42.85	67
Carbon nanotubes (CNTs) composite	50.75	68
NaX/MgO–TiO_2 zeolite nanocomposite	53.76	69
BHec-40	117.71	This work

Adsorption thermodynamics. The thermodynamic parameters of MO adsorption on BHec-40 were determined by the value of enthalpy, entropy, and Gibbs free energy. These thermodynamic parameters can be calculated using the Van't Hoff equation by plotting $\ln K_c$ on the y-axis and $1/T$ on the x-axis, as shown in Fig. 13.

Based on the graph in Fig. 13, the values of enthalpy ($\Delta H°$) and entropy ($\Delta S°$) can be calculated using the slope and intercept of the obtained linear curve. Then the value of Gibbs free energy ($\Delta G°$) is obtained from calculations using eqn (2). The thermodynamic parameters obtained from the $\ln K_c$ *vs.* $1/T$ graph are shown in Table 6.

The values of $\Delta H°$ and $\Delta S°$ are greater than zero, as shown in Table 6. A positive ΔH value indicates that the adsorption of MO to BHec-40 is an endothermic process and physical process involving weak attractive forces.[1] Meanwhile, the $S° > 0$ implies an increased irregularity of the adsorbent at high temperature and the solid-solution randomness during adsorption. Observations show that increasing temperature causes structural changes in the active sites of hectorite and methyl orange.[70] The negative value of Gibbs energy ($\Delta G°$) of MO adsorption indicates that the adsorption takes place spontaneously and without using external energy for the adsorption process.[52] The value of

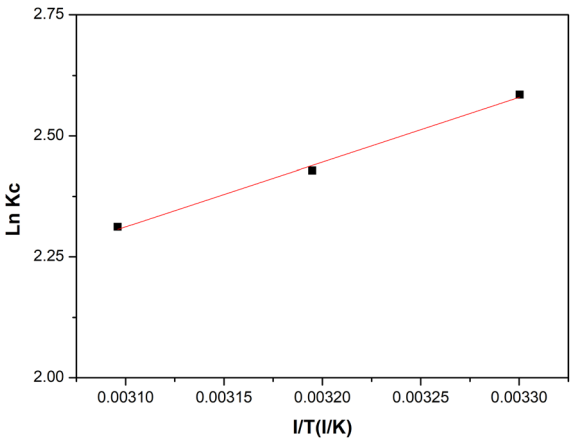

Fig. 13 The Van't Hoff plot of MO adsorption on BHec-40.

Table 6 Thermodynamic parameters associated with the adsorption of MO by BHec-40

T (K)	$-\Delta G°$ (kJ mol^{-1})	$\Delta H°$ (kJ mol^{-1})	$\Delta S°$ (J mol^{-1} K^{-1})	E_a (kJ mol^{-1})
303	4.616	11.13	15.27	2.62
313	4.768			
323	4.921			

$\Delta G°$ explains the process of MO adsorption into BHec-40. When $\Delta G°$ is between −20 to 0 kJ mol^{-1}, the adsorption is physical process. However, $\Delta G°$ between 80 to 400 kJ mol^{-1} indicates the chemisorption process.[61] In addition, the small E_a value of 2.62 kJ mol^{-1} demonstrates that MO adsorption on BHec-40 is a physisorption process.

Reusability study and scale-up operation. The reusability of adsorbents contributes significantly to the development of effective technologies for wastewater treatment plants. In five consecutive adsorption–desorption–desorption cycles, methanol was used as an eluent agent in the desorption and regeneration investigations. The removal percentage declined from 99.65% to 62.40% after five cycles, as shown in Fig. 14. MO's adsorption and desorption efficiency onto BHec-40 dropped to 62.40% and 55.58% after five cycles. This investigation demonstrated the successful regeneration of BHec-40 as an adsorbent for removing methyl orange from contaminated water.

The feasibility of BHec-40 adsorbent on an industrial scale is determined by modifying eqn (1) using the Langmuir isotherm model.[30,71] The K_L and q_{max} values from the Langmuir isotherm equation are used to obtain the correlation between the mass of the adsorbent and the volume of the adsorbate by modifying eqn (5). Modification of eqn (1) and (5) will show the relationship between the mass of the adsorbent and the volume of waste that can be overcome, as shown in eqn (15) and (16).

$$\frac{m}{V} = \frac{1}{q_e}(C_o - C_e) \quad (15)$$

q_e from eqn (5) is substituted into eqn (15):

$$\frac{m}{V} = \frac{1 + C_e K_L}{K_L C_e q_{max}}(C_o - C_e) \quad (16)$$

Eqn (16) determines the amount of BHec-40 required to remove 99% of the MO (50 mg L^{-1}). The calculations showed that 2.278 g of BHec-40 was needed to remove 1 L of MO solution.

Based on eqn (16), shows that BHec-40 is effective for treating MO waste. Easy synthesis and abundant raw materials make BHec-40 a prospective MO adsorbent. Zhang 2019 (ref. 17) reported that hectorite is a type of clay that is easy to synthesize hydrothermally in laboratories and industries and even modification of hectorite charge is easy to do both bottom-up[71] and top-down.[41] Furthermore, the hectorite synthesis stage does not produce chemical waste, in contrast to some of the adsorbents in Table 5 which produce strong acidic and basic wastes, such as in the chitosan isolation stage.[65] Regarding the production cost of hectorite, we cannot determine the amount. However, one of the commercially available hectorite products (LAPONITE®) can be purchased for only €70.21 per kilogram. This suggests that hectorite production is low-cost.

Proposed mechanism adsorption of MO using BHec-40. According to the literature, methyl orange is adsorbed to various adsorbents mainly *via* an electrostatic mechanism. MO interacts with adsorbents through the negatively charged sulfonate group of methyl orange with the cationic groups on adsorbents.[72] The FTIR spectra of BHec-40 recovered after methyl orange adsorption are presented in Fig. 15. Methyl orange showed the FTIR absorptions peak at 1609 cm^{-1}, ascribed to azo vibration (R–N=N–R). The peak at 1370 cm^{-1} indicates the sulphate vibrations ($-SO_3^-$). Additionally, the C–H vibration appeared at 1511 cm^{-1}, aromatic vibration at 819 cm^{-1}, and C–S stretching at 696 cm^{-1}. BHec-40 after MO adsorption showed similar adsorption bands with methyl orange at 1602, 1514, 1365, 825, and 696–624 cm^{-1}, indicating

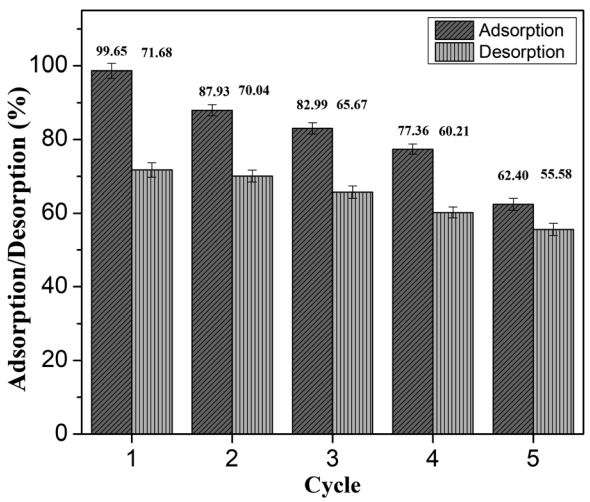

Fig. 14 Adsorption–desorption cycles of MO using beads of BHec-40.

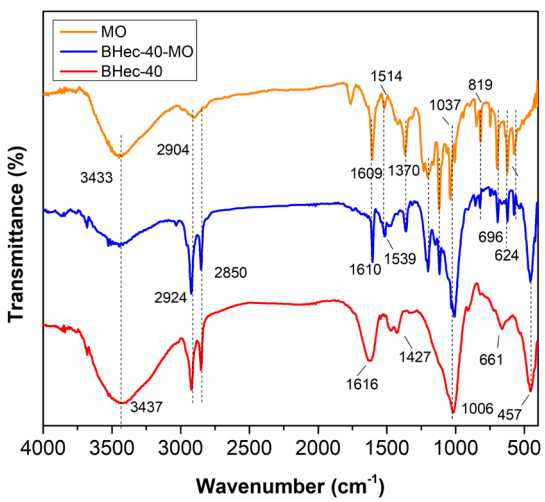

Fig. 15 The FTIR spectra of BHec-40, BHec-40 after MO adsorption.

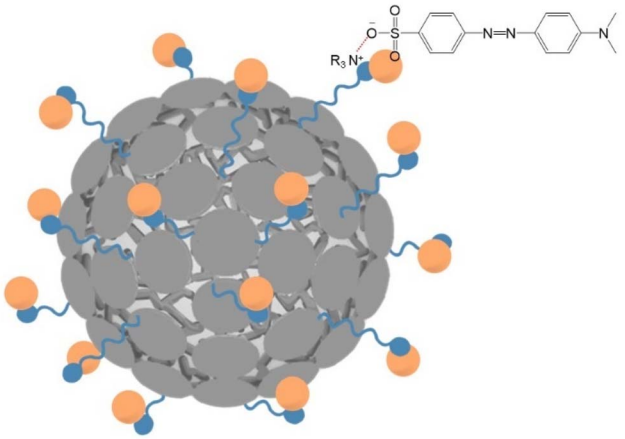

Fig. 16 Illustration of interaction between BHec-40 and MO.

the appearances of –N=N–, C–H (C=C–H), $-SO_3^-$, C–H aromatics, and C–S bonds.[73]

The ionic interaction between the sulfonate group MO and the cationic site CTAB was confirmed on the modified coffee waste adsorbent (MCWs), where there was a new peak at a wave number of 1607 cm^{-1} which indicated the stretching vibration of the azo group (–N=N–), and a wave number of 1195 cm^{-1} indicates the –S=O strain of the sulfonate group.[50] These two wave numbers (1607 cm^{-1} and 1195 cm^{-1}) are also found in BHec-40-MO. The presence of –S=O in BHec-40-MO indicates that the $-SO_3^-$ group is involved in the adsorption process. It can be proposed that the adsorption mechanism of MO into BHec-40 occurs through (i) electrostatic interaction between the $-SO_3^-$ group of MO and $R-N^+(CH_3)_3$ of CTAB, and (ii) hydrophobic–hydrophobic interaction between the methyl orange aromatic moiety and the CTAB chain.[1,50,71] The interaction between BHec-40 and methyl orange was illustrated in Fig. 16.

The interaction between methyl orange and BHec-40 was further evident by SEM-EDS analysis after the adsorption of methyl orange in Fig. 17. Sulphur which originated from methyl orange was analysed at 4.45% on BHec-40 after the adsorption process. In addition, the carbon content of BHec-40-MO increased 16.49%, compared to BHec-40 at 11.39% (Table 1).

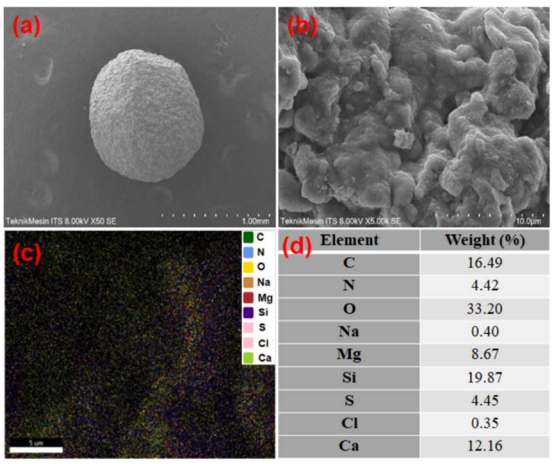

Element	Weight (%)
C	16.49
N	4.42
O	33.20
Na	0.40
Mg	8.67
Si	19.87
S	4.45
Cl	0.35
Ca	12.16

Fig. 17 SEM analysis of BHec-40 after adsorption with methyl orange (a and b); EDS elemental mapping (c); and the elemental composition (d).

Author contributions

Asranudin: conceptualization, methodology, investigation, validation, writing – original draft. Holilah: methodology, validation, supervision, writing – review & editing. Adi Setyo Purnomo: supervision, validation, writing – review & editing. Hasliza Bahruji: conceptualization, supervision, validation. Dalia Allouss: investigation, writing – review & editing. El Alaoui-Elbalrhiti: writing – review & editing. Riki Subagyo: validation, conceptualization. Alya Awinatul Rohmah: validation, conceptualization. Didik Prasetyoko: validation, supervision, writing – review & editing.

Conflicts of interest

There are no conflicts to declare.

Acknowledgements

The authors convey sincere thanks to the Kementerian Pendidikan, Kebudayaan, Riset, dan Teknologi Indonesia for their financial support through the Penelitian Disertasi Doktor (PDD) Programme fund under contract number 008/E5/PG.02.00.PT/2022 and 1571/PKS/ITS/2022.

Notes and references

1 A. R. P. Hidayat, D. O. Sulistiono, I. K. Murwani, B. F. Endrawati, H. Fansuri, L. L. Zulfa and R. Ediati, *J. Environ. Chem. Eng.*, 2021, **9**(6), 106675.
2 B. J. Brüschweiler and C. Merlot, *Regul. Toxicol. Pharmacol.*, 2017, **88**, 214–226, DOI: 10.1016/j.yrtph.2017.06.012.
3 V. V. K. Madhava Anil Kumar, S. Poonam, D. A. Gurunathan Baskar, M. Seenuvasan and S. Sivanesane, *Process Biochem.*, 2017, **57**, 81–189, DOI: 10.1016/j.procbio.2017.03.012.
4 D. Olivo-Alanis, R. B. Garcia-Reyes, L. H. Alvarez and A. Garcia-Gonzalez, *J. Hazard. Mater.*, 2018, **347**, 423–430, DOI: 10.1016/j.jhazmat.2018.01.019.
5 J. Sun, J. Jin, R. D. Beger, C. E. Cerniglia and H. Chen, *J. Ind. Microbiol. Biotechnol.*, 2017, **44**(10), 471–1481, DOI: 10.1007/s10295-017-1970-8.
6 D. Baena-baldiris, A. Montes-robledo and R. Baldiris-avila, *Omega*, 2020, **5**, 28146–188157, DOI: 10.1021/acsomega.0c03786.
7 N. Patel, B. Soni and J. P. Ruparelia, *Nirma Univ. J. Eng. Technol.*, 2010, **1**(1), 20–25.
8 S. S. Moghaddam, M. R. A. Moghaddam and M. Arami, *J. Hazard. Mater.*, 2010, **175**, 651–657, DOI: 10.1016/j.jhazmat.2009.10.058.
9 J. Marszałek and R. Zyłła, *Processes*, 2021, **9**(1833), 1–15.

10 Z. Shuangxi, D. Zhiling, L. Xiuwen, Z. Yunhai, H. Yide and Z. Yongjun, *R. Soc. Open Sci.*, 2019, **6**, 7, DOI: 10.1098/rsos.190351.
11 A. A. Beddai, B. A. Badday, A. M. Al-yaqoobi, M. K. Mejbel, Z. S. Al Hachim and M. K. A. Mohammed, *Int. J. Chem. Eng.*, 2022, 1–8.
12 M. Guadalupe, A. María, L. Fiasconaro and M. Eugenia, *SN Appl. Sci.*, 2020, **2**(5), 1–15, DOI: 10.1007/s42452-020-2824-y.
13 D. Allouss, Y. Essamlali, O. Amadine, A. Chakir and M. Zahouily, *RSC Adv.*, 2019, **9**(65), 37858–37869, DOI: 10.1039/c9ra06450h.
14 M. Rajabi, K. Mahanpoor and O. Moradi, *RSC Adv.*, 2017, **7**(74), 47083–47090, DOI: 10.1039/c7ra09377b.
15 H. S. Santos, *et al.*, *Appl. Sci.*, 2017, **7**, 12, DOI: 10.3390/app7121243.
16 D. Tong, K. Fang, H. Yang, J. Wang, C. Zhou and W. Yu, *Environ. Sci. Pollut. Res.*, 2019, **26**(16), 16482–16492, DOI: 10.1007/s11356-019-04895-8.
17 J. Zhang, C. H. Zhou, S. Petit and H. Zhang, *Appl. Clay Sci.*, 2019, **177**, 114–138, DOI: 10.1016/j.clay.2019.05.001.
18 R. R. Pawar, Lalhmunsiama, P. Gupta, S. Y. Sawant, B. Shahmoradi and S. M. Lee, *Int. J. Biol. Macromol.*, 2018, **114**, 1315–1324, DOI: 10.1016/j.ijbiomac.2018.04.008.
19 R. R. Pawar, B. D. Kevadiya, H. Brahmbhatt and H. C. Bajaj, *Int. J. Pharm.*, 2013, **446**(1–2), 145–152, DOI: 10.1016/j.ijpharm.2013.02.021.
20 C. Zhou, D. Tong and X. Li, Synthetic Hectorite: Preparation, Pillaring and Applications in Catalysis, in *Pillared Clays and Related Catalysts*, ed. A. Gil, S. A. Korili, R. Trujillano and M. A. Vicente, Springer, New York, NY, 2010, pp. 67–97.
21 F. de Castro Silva, L. C. Brandão Lima, E. C. Silva-Filho, M. G. Fonseca and M. Jaber, *Colloids Surf., A*, 2020, **587**, 124323, DOI: 10.1016/j.colsurfa.2019.124323.
22 C. Xia, Y. Jing, Y. Jia, D. Yue, J. Ma and X. Yin, *Desalination*, 2011, **265**(1–3), 81–87, DOI: 10.1016/j.desal.2010.07.035.
23 P. Baskaralingam, M. Pulikesi, V. Ramamurthi and S. Sivanesan, *Appl. Clay Sci.*, 2007, **37**(1–2), 207–214, DOI: 10.1016/j.clay.2007.01.014.
24 K. Vijayalakshmi, *et al.*, *Int. J. Biol. Macromol.*, 2017, **104**, 1483–1494, DOI: 10.1016/j.ijbiomac.2017.04.120.
25 A. Nasrullah, A. H. Bhat, A. Naeem, M. H. Isa and M. Danish, *Int. J. Biol. Macromol.*, 2018, **107**, 1792–1799, DOI: 10.1016/j.ijbiomac.2017.10.045.
26 A. Benhouria, M. A. Islam, H. Zaghouane-Boudiaf, M. Boutahala and B. H. Hameed, *Chem. Eng. J.*, 2015, **270**, 621–630, DOI: 10.1016/j.cej.2015.02.030.
27 W. Li, Q. Ma, Y. Bai, D. Xu, M. Wu and H. Ma, *Chem. Eng. Res. Des.*, 2018, **134**, 336–346, DOI: 10.1016/j.cherd.2018.04.016.
28 W. Wang, Y. Zhao, H. Bai, T. Zhang, V. Ibarra-Galvan and S. Song, *Carbohydr. Polym.*, 2018, **198**, 518–528, DOI: 10.1016/j.carbpol.2018.06.124.
29 K. O. Iwuozor, J. O. Ighalo, E. C. Emenike, L. A. Ogunfowora and C. A. Igwegbe, *Curr. Res. Green Sustainable Chem.*, 2021, **4**, 00179, DOI: 10.1016/j.crgsc.2021.100179.
30 H. Mondal, M. Karmakar, P. Kanti and A. Halder, *J. Hazard. Mater.*, 2021, **409**, 124873, DOI: 10.1016/j.jhazmat.2020.124873.
31 I. Hasan and R. Ahamd, *Groundw. Sustain. Dev.*, 2019, **8**, 82–92, DOI: 10.1016/j.gsd.2018.09.003.
32 R. Subagyo, *et al.*, *Arabian J. Chem.*, 2022, **15**, 103754, DOI: 10.1016/j.arabjc.2022.103754.
33 A. Qayoom, S. Arif Kazmi and S. Nadir Ali, *Moroccan J. Chem.*, 2017, **5**, 362–370.
34 T. Hellna, R. Subagyo and Y. Kusumawati, *Sustainable Environ. Res.*, 2022, **32**(4), 1–12.
35 P. Pal, S. S. Syed and F. Banat, *J. Water Process. Eng.*, 2017, **20**, 40–50, DOI: 10.1016/j.jwpe.2017.09.010.
36 I. Fatimah, Narsito and K. Wijaya, *ITB J. Sci.*, 2011, **43**(2), 123–138, DOI: 10.5614/itbj.sci.2011.43.2.5.
37 T. Sánchez, P. Salagre and Y. Cesteros, *Microporous Mesoporous Mater.*, 2013, **171**, 24–34, DOI: 10.1016/j.micromeso.2013.01.001.
38 G. Sethia, H. A. Patel, R. R. Pawar and H. C. Bajaj, *Appl. Clay Sci.*, 2014, **91–92**, 63–69, DOI: 10.1016/j.clay.2014.01.019.
39 Y. Yang, *et al.*, *J. Colloid Interface Sci.*, 2013, **410**, 27–32, DOI: 10.1016/j.jcis.2013.07.060.
40 M. Guo, *et al.*, *Clays Clay Miner.*, 2020, **68**(6), 646–655, DOI: 10.1007/s42860-020-00093-7.
41 Z. Huang, *et al.*, *Mater. Chem. Phys.*, 2017, **202**, 266–276, DOI: 10.1016/j.matchemphys.2017.09.028.
42 E. Torres, Y. N. Mata, M. L. Blázquezy, J. A. Muñoz, F. González and A. Ballester, *Langmuir*, 2005, **21**, 17.
43 W. M. Algothmi, N. M. Bandaru, Y. Yu, J. G. Shapter and A. V. Ellis, *J. Colloid Interface Sci.*, 2013, **397**, 32–38, DOI: 10.1016/J.JCIS.2013.01.051.
44 Lalhmunsiama, R. R. Pawar, S. M. Hong, K. J. Jin and S. M. Lee, *J. Mol. Liq.*, 2017, **240**, 497–503, DOI: 10.1016/J.MOLLIQ.2017.05.086.
45 R. R. Pawar, H. A. Patel, G. Sethia and H. C. Bajaj, *Appl. Clay Sci.*, 2009, **46**(1), 109–113, DOI: 10.1016/j.clay.2009.07.009.
46 V. F. T. Teixeira, N. R. Pereira, W. R. Waldman, A. L. C. D. Ávila, V. H. Pérez and R. J. S. Rodríguez, *Carbohydr. Polym.*, 2014, **111**, 198–205, DOI: 10.1016/J.CARBPOL.2014.04.009.
47 A. S. Purnomo, Asranudin, N. Rachmawati, H. D. Rizqi, R. Nawfa and S. R. Putra, *HAYATI J. Biosci.*, 2022, **29**(2), 146–154, DOI: 10.4308/hjb.29.2.146-154.
48 A. A. Jalil, *et al.*, *J. Hazard. Mater.*, 2010, **181**(1–3), 755–762, DOI: 10.1016/j.jhazmat.2010.05.078.49.
49 D. Yang, L. Qiu and Y. Yang, *J. Chem. Eng. Data*, 2016, **61**(11), 3933–3940, DOI: 10.1021/acs.jced.6b00706.
50 R. Lafi and A. Hafiane, *J. Taiwan Inst. Chem. Eng.*, 2016, **58**, 424–433, DOI: 10.1016/j.jtice.2015.06.035.
51 V. V. Dawkar, U. U. Jadhav, G. S. Ghodake and S. P. Govindwar, *Biodegradation*, 2009, **20**(4), 777–787, DOI: 10.1007/s10532-009-9266-y.
52 H. Tehubijuluw, *et al.*, *Environ. Sci. Pollut. Res.*, 2021, **28**, 37354–37370, DOI: 10.1007/s11356-021-13285-y.
53 E. Santoso, R. Ediati, Z. Istiqomah and D. Oktavia, *Microporous Mesoporous Mater.*, 2020, **310**, 110620, DOI: 10.1016/j.micromeso.2020.110620.
54 A. A. Rohmah, A. S. Purnomo and Asranudin, in *Sriwijaya Conference on Sustainable Environment, Agriculture and*

Farming System, 2022, pp. 8–14, DOI: 10.1088/1755-1315/995/1/012046.

55 Ravi and L. M. Pandey, *Appl. Clay Sci.*, 2019, **169**, 102–111, DOI: 10.1016/j.clay.2018.12.019.

56 F. Ayari, G. Manai, S. Khelifi and M. Trabelsi-Ayadi, *J. Saudi Chem. Soc.*, 2019, **23**(3), 294–306, DOI: 10.1016/j.jscs.2018.08.001.

57 T. A. Nguyen, C. C. Fu and R. S. Juang, *Chem. Eng. J.*, 2016, **304**, 313–324, DOI: 10.1016/j.cej.2016.06.102.

58 L. Qian, M. Ma and D. Cheng, *J. Mol. Liq.*, 2014, **197**, 295–300, DOI: 10.1016/j.molliq.2014.05.026.

59 K. Yang, *et al.*, *Mater. Res. Express*, 2020, **7**, 015103.

60 A. Romadhoni, *et al.*, *J. Environ. Chem. Eng.*, 2022, **10**(3), 107505, DOI: 10.1016/j.jece.2022.107505.

61 R. Lafi, L. Abdellaoui, I. Montasser, W. Mabrouk and A. Hafiane, *J. Mol. Struct.*, 2022, **1249**, 131527, DOI: 10.1016/j.molstruc.2021.131527.

62 P. K. Sharma, S. Ayub and C. N. Tripathi, *Cogent Eng.*, 2016, **3**(1), 1186857, DOI: 10.1080/23311916.2016.1186857.

63 K. Mishima, X. Du, N. Miyamoto, N. Kano and H. Imaizumi, *J. Funct. Biomater.*, 2018, **9**(3), 49, DOI: 10.3390/jfb9030049.

64 A. Kara and E. Demirbel, *Water, Air, Soil Pollut.*, 2012, **223**, 2387–2403, DOI: 10.1007/s11270-011-1032-1.

65 V. S. Munagapati, V. Yarramuthi and D. S. Kim, *J. Mol. Liq.*, 2017, **240**, 329–339, DOI: 10.1016/j.molliq.2017.05.099.

66 P. Zhao, R. Zhang and J. Wang, *Water Sci. Technol.*, 2017, 1–10, DOI: 10.2166/wst.2017.034.

67 A. Ahmad, *et al.*, *Chemosphere*, 2017, **168**, 474–482, DOI: 10.1016/j.chemosphere.2016.11.028.

68 J. Chen, X. Shi, Y. Zhan, X. Qiu, Y. Du and H. Deng, *Appl. Surf. Sci.*, 2017, **397**, 133–143, DOI: 10.1016/j.apsusc.2016.10.211.

69 D. Mirzaei, A. Zabardasti, Y. Mansourpanah, M. Sadeghi and S. Farhadi, *J. Inorg. Organomet. Polym. Mater.*, 2020, **30**(6), 2067–2080, DOI: 10.1007/s10904-019-01369-9.

70 M. Abbas and M. Trari, *Process Saf. Environ. Prot.*, 2015, **98**, 424–436.

71 Asranudin, A. S. Purnomo, D. Prasetyoko, H. Bahruji and Holilah, *Mater. Chem. Phys.*, 2022, **291**, 126749, DOI: 10.1016/j.matchemphys.2022.126749.

72 D. J. Ramírez, L. A. A. Herrera, R. Colorado-Peralta, R. P. Rodríguez, P. K. C. Reyes, L. E. Chiñas, M. Sánchezd and J. M. Rivera, *R. Soc. Chem.*, 2021, **23**, 3537–3548, DOI: 10.1039/d0ce00741b.

73 L. Wu, X. Liu, G. Lv, R. Zhu, L. Tian, M. Liu, Y. Li, W. Rao, T. Liu and L. Liao, *Sci. Rep.*, 2021, **11**, 10640, DOI: 10.1038/s41598-021-90235-1.